Energy Storage Materials xxx (xxxx) xxx–xxx

Contents lists available at ScienceDirect

Energy Storage Materials

journal homepage: www.elsevier.com/locate/ensm

Tri-high designed graphene electrodes for long cycle-life supercapacitors with high mass loading

Tieqi Huang, Xingyuan Chu, Shengying Cai, Qiuyan Yang, Hao Chen, Yingjun Liu, Karthikeyan Gopalsamy, Zhen Xu, Weiwei Gao, Chao Gao*

MOE Key Laboratory of Macromolecular Synthesis and Functionalization, Department of Polymer Science and Engineering, Key Laboratory of Adsorption and Separation Materials & Technologies of Zhejiang Province, Zhejiang University, 38 Zheda Road, Hangzhou 310027, PR China

ABSTRACT

Practical supercapacitor electrodes require high mass loading to enhance the energy density of the entire devices, which would limit ion diffusions in thicker electrodes and thus generally result in poor specific capacitance, rate capability and cycle life. Here, we demonstrate a "highly oriented, highly crumpled and highly doped" (3H) design for fabrication of high mass loading yet high performance nitrogen-doped graphene film (NGF) electrodes. NGF exhibits a unique long-range orientating and short-range crumpling structure, ensuring high packing density (up to 1.64 g cm^{-3}) and efficient ion transmission simultaneously. The NGF-based symmetric supercapacitors (NGF-SC) displayed a specific capacitance 413 F cm^{-3} or 252 F g^{-1} at areal mass loading 0.32 mg cm^{-2}, and 370 F cm^{-3} or 226 F g^{-1} at 11.2 mg cm^{-2} in aqueous electrolyte. For the case of high mass loading (11.2 mg cm^{-2}), 90.1% retention was achieved after 100,000 cycles. In ionic liquid, the NGF-SC showed a high specific capacitance 352 F cm^{-3} or 215 F g^{-1} at 11.2 mg cm^{-2} in potential window 0–3.5 V, affording an ultrahigh electrode-based energy density 138 W h L^{-1}. Due to the 3H design and high mass loading, the energy density of the whole NGF-SC device attains 65 W h L^{-1}, much higher than those of commercial supercapacitors. Notably, such NGF-SC showed long lifespan up to 50,000 cycles with 84.8% retention, a record cycle-life for high mass loading supercapacitors. The 3H design provides a constructive principle for production of practical supercapacitors with both high energy density and power density.

1. Introduction

The increasing demands on consumer electronics (CEs) and electric vehicles (EVs) in modern society raise enormous effects on energy storage and supply systems including supercapacitors [1,2]. Supercapacitors store energy mainly through highly reversible ion adsorption and desorption on the electrode surface, which contribute extremely high power density while suffer low energy density problems [3–5]. In this regard, considerable efforts have been made to increase the energy density of electrodes, while most of them usually possess low mass loading (< 5 mg cm^{-2}) and nanoscale dimensions [6–9]. High mass loading (> 10 mg cm^{-2}) of the electrode is actually necessary in order to offset the negative contribution of inactive materials (such as current collectors and separators in practical devices) on the overall performance [10–18]. Unfortunately, with increasing mass loading, the device performance usually decreases sharply and the cycling life was also somehow limited [19–21]. Furthermore, devices with high mass loading are usually assembled with aqueous electrolyte, which demonstrate relatively narrow potential window (< 2 V) compared to these with organic electrolyte (> 2.5 V) and thus lower energy density [22]. In addition, although some researchers like Yang have taken cognizance of the importance of electrode packing density [10], current devices usually have a low packing density with huge space in the electrodes and hence resulting in a relative low volumetric capacitance [11,12,23,24]. Despite of the demonstration of four factors that are important to the volumetric performance (the specific capacitance of the materials, the operation voltage, the density and thickness of the electrodes) [25], there is still no precise and direct principle to guide us to prepare practical devices with high volumetric performance. Therefore, achieving supercapacitor devices with impressive mass loading, wide potential window and high packing density aiming for high energy density and long lifespan is still in urgent need.

Here, we demonstrate a fabrication strategy of graphene electrodes guided by the "highly oriented, highly crumpled and highly doped" (3H) design. With a scalable two-step method including wet-spinning technology and hydrothermal reaction, free-standing nitrogen-doped

* Corresponding author.
E-mail address: cgao18@163.com (C. Gao).

https://doi.org/10.1016/j.ensm.2018.07.001
Received 27 April 2018; Received in revised form 30 June 2018; Accepted 1 July 2018

graphene film (NGF) with a high density of 1.64 ± 0.05 g cm^{-3} has been prepared. The NGF-based symmetric supercapacitors (NGF-SC) displayed a specific capacitance 413 F cm^{-3} or 252 F g^{-1} at areal mass loading 0.32 mg cm^{-2}, and 370 F cm^{-3} or 226 F g^{-1} at 11.2 mg cm^{-2} in aqueous electrolyte. Even with the high mass loading of 11.2 mg cm^{-2}, 90.1% retention was still achieved of NGF-SC after 100,000 cycles. Remarkably, as ionic liquid electrolyte was introduced, the NGF-SC showed a high specific capacitance 352 F cm^{-3} or 215 F g^{-1} at 11.2 mg cm^{-2} in a broad potential window 0–3.5 V, resulting in an ultrahigh electrode-based energy density 138 W h L^{-1}. Taking advantages of the 3 H design and high mass loading, the energy density of the whole device can achieve 65 W h L^{-1}, which is much higher than the commercial carbon based supercapacitors (5~8 W h L^{-1}) [26]. Impressively, the NGF-SC with mass loading of 11.2 mg cm^{-2} can still display 84.8% retention after 50,000 charge and discharge cycles in ionic liquid electrolyte, which is the best record among reported supercapacitors with high mass loading and high potential window. We attribute the excellent performance to the unique "long-range orientating, short-range crumpling" (LOSC) structure introduced by the 3H design: long-range orientating ensures continuous conductive networks, and short-range crumpling provides efficient ions pathways. The 3H design establishes a bridge to solve the traditional mismatches between high electrochemical performance and mass loading, leading to a satisfactory energy storage performance and service life.

2. Results and discussion

2.1. Tri-High designed graphene film

Fig. 1a shows the 3H design schematically. From the macroscopic view, the film electrode needs to be highly oriented, not only to ensure the high conductivity but also to increase the packing density. From the microscopic view, the inner structure of the film electrode needs to be highly crumpled to supply adequate ion transmission pathways, which guarantees the effective connection between electrolyte and electrodes. From the atomic view, the graphene sheets need to be highly doped to introduce pseudocapacitance and further destroy the restacking microstructures. For these purposes, we fabricated NGF through a wet-spinning technology combined with a further hydrothermal reaction (Fig. 1b). Liquid crystal graphene oxide (GO) aqueous solution in a proper concentration (~ 15 mg mL^{-1}), which is suitable for wet-spinning [27–29], was spun into the precipitation bath (water: ethanol = 3:1, NH_4HCO_3:10 wt%), affording continuous hydrogel films. Subsequent hydrothermal treatment in the NH_4HCO_3 bath gave rise to black NGF with considerable conductivity (~ 2200 S m^{-1}). Fig. 1c shows a semi-unfolded graphene film roll with length of 30 cm. It also exhibited certain flexibility that can be rolled up without breakage as shown in Fig. 1d, indicating its potential as a free-standing electrode. This 3 H design strategy is much more productive than the reported electrode preparations, such as the binder-containing filming [30], freeze-drying assembly [31], chemical vapor deposition (CVD) [32] and filtration [33].

2.2. Characterization of NGF and GF

As the prove of concept, scanning electron microscopy (SEM) images showed the typical microstructures of NGF with a long-range oriented RGO layers at low magnification (Fig. 2a), which is similar to the literatures of neat graphene or graphene oxide films [34–36]. As further zooming in, the expected crumpled structure with 'w' shaped RGO sheets (Fig. 2b) was clearly observed. In contrast, only serious restacking of layered RGO sheets but no apparent crumples was formed in the case of GF (Fig. 2c, d). This phenomenon indicates that NH_4HCO_3 acted as the pore-forming agent as the crumpled microstructure formation.

Mechanical measurements (Fig. 2e) demonstrate that NGF with crumpled microstructures holds a higher fracture elongation (~ 1.25%) while a bit lower tensile stress (~ 18 MPa) than these of GF (~ 1.01% and ~ 24 mPa, respectively). This can be attributed to the crumpled microstructures of NGF, comparing with the re-stacking microstructure of GF [37]. X-ray diffraction (XRD) is also used to further prove the crumpled structure (Fig. S1). Although both NGF and GF display main (002) peak around 25°, the peak width at half height of NGF is obviously larger than that of GF. This means the lower crystallinity of NGF due to the more disordering structure than in the case of GF [38].

In the meantime, the NGF reached an high density up to 1.64 ± 0.05 g cm^{-3}, higher than the state-of-the-art reported graphene-based materials for energy storage [10,11,26,39], benefitting from the flow induced orientation of GO liquid crystal during wet-spinning process. However, in the absence of pore-forming agent, NH_4HCO_3 here, the gas originated from the hydrothermal reduction will gather into huge bubbles between the interlayers, which left a big cavity in GF after the gas released (Fig. S2) [40]. This explains the lower density of GF (1.47 ± 0.07 g cm^{-3}) than that of NGF. The nitrogen adsorption experiments gave some clue for the explanation of above mentioned phenomenon. The total pore volume of NGF is only 0.169 cm^3 g^{-1}, indicating that the shrinkage of our NGF is serious, which thus explained why the theoretical density (1.63 g cm^{-3}, see the Supporting information) of NGF was also higher than that of reported graphene macroform (1.58 g cm^{-3}) [10]. Fig. 2f demonstrates that both NGF and GF perform a combination isotherm of Type II and Type IV with similar specific surface area (114 m^2 g^{-1} for NGF and 102 m^2 g^{-1} for GF). According to

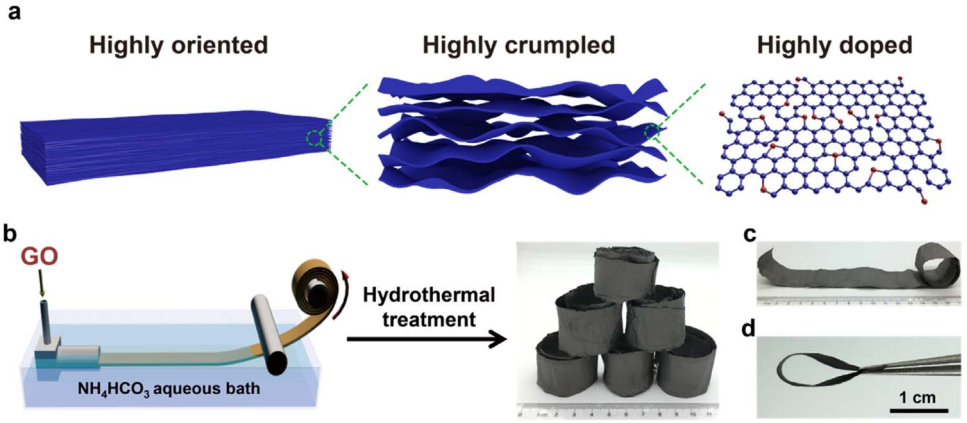

Fig. 1. (a) Schematic of the "highly oriented, highly crumpled and highly doped" (3H) design. Blue ball: carbon, red ball: nitrogen. (b) Schematic of the scalable preparation of NGF. (c) Optical image of the semi-unfolding NGF roll. (d) Optical image of the NGF with bending state (For interpretation of the references to color in this figure legend, the reader is referred to the web version of this article.).

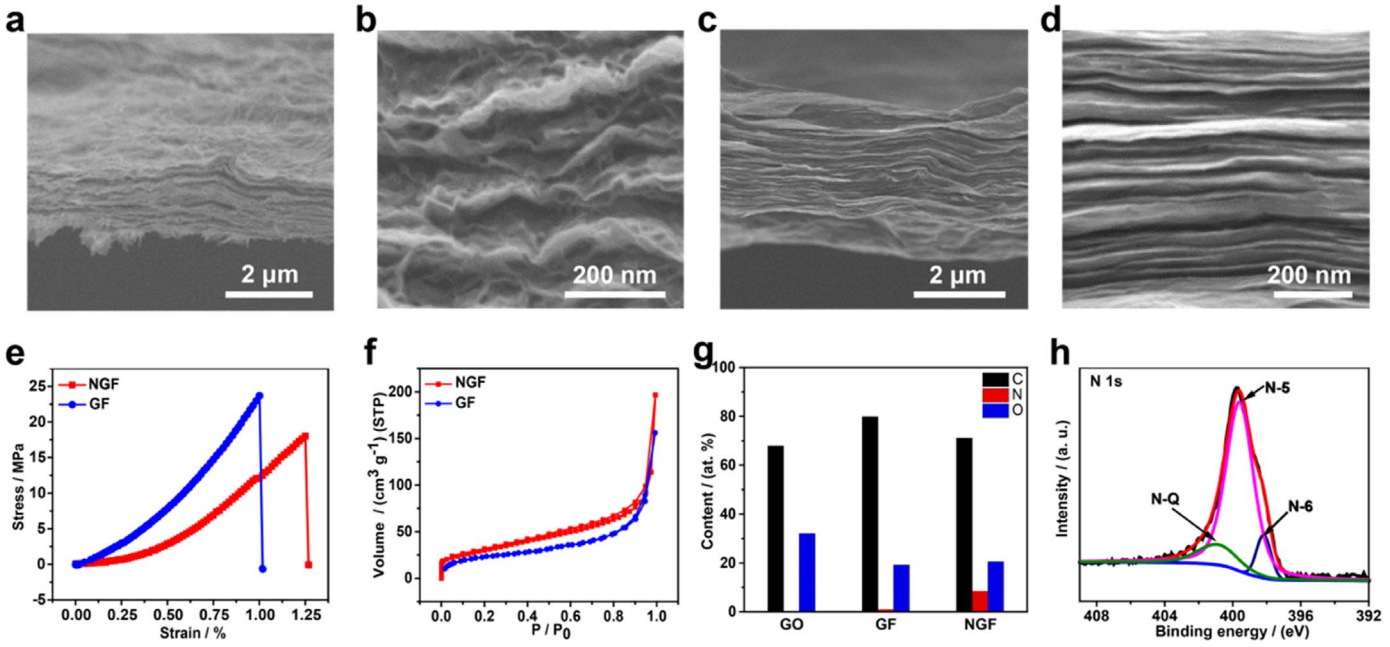

Fig. 2. (a, b) Cross-section SEM images of NGF with different magnifications. (c, d) Cross-section SEM images of GF with different magnifications. (e) Mechanical measurements of NGF and GF. (f) Nitrogen adsorption isotherms of NGF and GF. (g) C, N and O element content in GO, GF and NGF based on XPS data. (h) XPS deconvolutions of the N 1s region of NGF.

the pore size distributions in Fig. S3, NGF and GF show different features in meso- and micropores: NGF displays more mesopores than GF, while it is the opposite of the micropore region. GF exhibits one diffusion peak around 1.09 nm in micropore part, indicating the uniform restacking microstructure. However, compared with GF, NGF presents another sharp peak around 0.69 nm. The small pore size (~ 0.69 nm) is estimated to be the result of incorporation of nitrogen-containing functional groups [41], while the large pore size (~ 1.47 nm) is speculated to be the result of the evolution of pores from the removal of trapped water and bound oxygen [10].

The nitrogen-doped carbon skeleton of NGF is confirmed by X-ray photoelectron spectroscopy (XPS). As shown Figs. 2g, 8.4 at% nitrogen is observed in NGF while there is almost no nitrogen content in GF (0.96 at%). The deconvolutions of the N 1s region spectrum to identify the surface functionalities are fitted by three component peaks (Fig. 2h), which are attributed to three types of nitrogen functional groups, namely pyridinic (398.2 eV, N-6), pyrrolic/pyridone (399.9 eV, N-5), quaternary nitrogen (400.9 eV, N-Q) [42,43]. The N-5 structure is dominant due to the mildly doped condition [44]. In addition, the obvious peaks of N-Q and N-6 demonstrate the successful nitrogen-

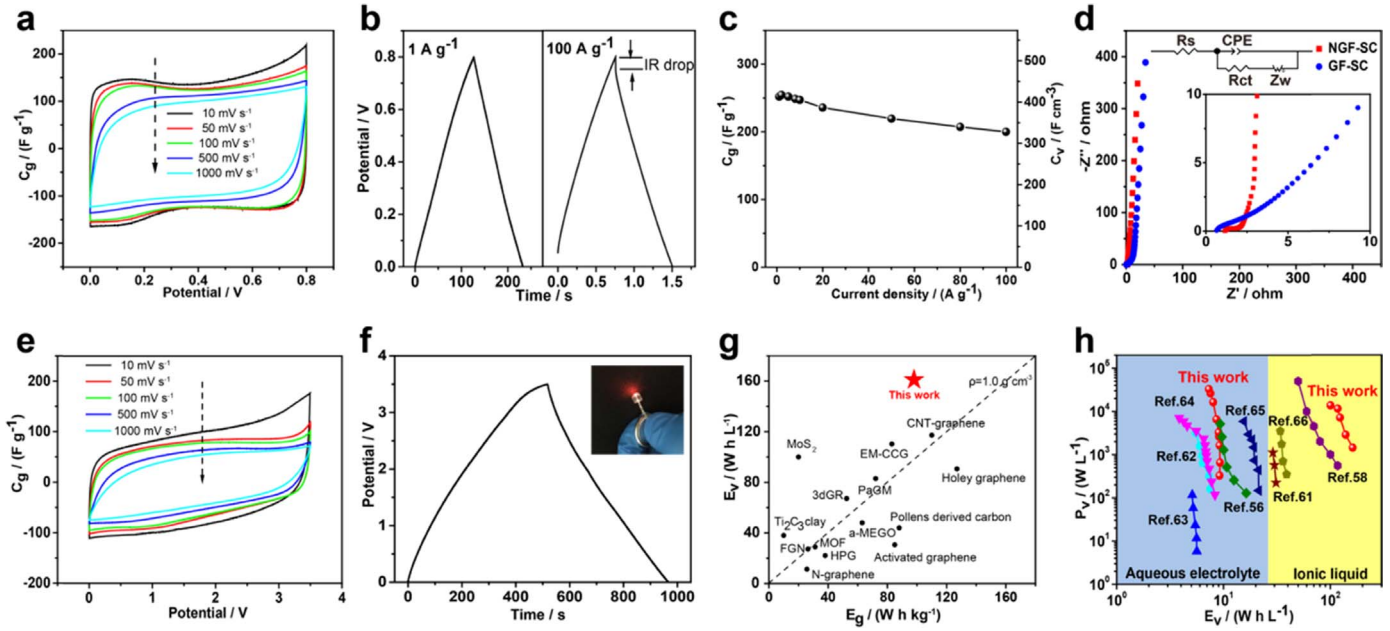

Fig. 3. (a) CV curves of NGF-SC measured at scan rates of 10, 50, 100, 500, 1000 mV s^{-1}. (b) GCD curves of NGF-SC measured at current densities of 1 and 100 A g^{-1}. (c) Rate capability of NGF-SC calculated by GCD curves from 1 to 100 A g^{-1}. (d) Nyquist plots of NGF-SC and GF-SC with the equivalent circuit, the inset shows the magnified high-frequency region. (e) CV curves of NGF-SC with $EMIMBF_4$ measured at scan rates of 10, 50, 100, 500, 1000 mV s^{-1}. (f) GCD curve of NGF-SC with $EMIMBF_4$ at the current density of 1 A g^{-1}, the inset shows a LED powered by a 3.5 V device assembled with symmetric NGF. (g) Comparison of E_g and E_v of NGF-SC with reported state-of-the-art materials, the data are all calculated from the active materials based on Refs. [11,26,50–61]. (h) Volumetric Ragone plots comparing NGF with reported carbonaceous electrodes in aqueous electrolyte and ionic liquid.

doping into the carbon skeleton [45]. To confirm the nitrogen doping, we have carried out the elemental analysis to correlate with the statements of XPS results (Table S1). Accordingly, the nitrogen content based on XPS data (8.4 at%) was similar to it calculated by elemental analysis (8.16 at%), which demonstrates the uniformly doping of nitrogen in the whole graphene film with the help of NH_3HCO_3.

2.3. Electrochemical performance

Fig. 3 exhibits the electrochemical performance of assembled two-electrode supercapacitors (Fig. S4) [46]. We employed 1 M H_2SO_4 as the aqueous electrolyte and free-standing NGF as electrodes. The cyclic voltammetry (CV) curves shown in Fig. 3a retain semi-rectangle shape even at the high scan rate of 1,000 mV s^{-1}, indicating the good capacitive behavior with high rate capacities for NGF electrodes. The galvanostatic charge and discharge (GCD) curves show semi-triangle shape from 1 to 100 A g^{-1} (Fig. 3b and Fig. S5), indicating well-combined electrical double layer capacitor (EDLC) behavior with pseudocapacitance. Accordingly, the gravimetric specific capacitance (C_g) and volumetric specific capacitance (C_v) of NGF electrodes reached up to 252 F g^{-1} and 413 F cm^{-3} at the current density of 1 A g^{-1}, listing on the top class of the previous reports (Table S2). The internal resistance (IR) drop of NGF-SC is only 0.05 V under the high current density of 100 A g^{-1}, indicating its low electrochemical resistance. The C_g and C_v still retained 200 F g^{-1} and 328 F cm^{-3} even if the current density increased to 100 A g^{-1} (Fig. 3c), indicating 79% retention as the current density increases 100 times. As a comparison, GF based supercapacitors (GF-SC) show leaf-shape curves when the scan rates increase, indicating inefficient ion responsibility (Fig. S6). Compared with NGF electrodes, GF electrodes show much lower C_g and C_v (191 F g^{-1} and 281 F cm^{-3} at 1 A g^{-1}), with only 33% capacitance retention (63 F g^{-1} and 106 F cm^{-3}) when the current density increases to 100 A g^{-1} (Fig. S7). These results demonstrate that the 3H design plays a key role in improving the capacitance and rate performance.

Electrochemical impedance spectroscopy (EIS) has been employed to investigate the resistance behavior of our supercapacitors. Equivalent series resistance (R_{ESR}) is mainly composed of three parts, i.e., the intrinsic ohmic resistance (R_s), the interfacial charge transfer resistance (R_{ct}), and the Warburg diffusion resistance (R_w) [7]. Both NGF-SC and GF-SC show nearly vertical Nyquist plots in the low frequency region (Fig. 3d), demonstrating the idea capacitive behavior originated from carbon framework [47]. The irefnset in Fig. 3d is the magnification of the high frequency region, exhibiting the detailed resistance. The NGF-SC shows slightly higher R_s (1.2 Ω) than GF-SC (0.92 Ω), resulting from the destruction of graphene restacking. However, compared with GF-SC, NGF-SC presents a tiny fraction in the R_{ct} and R_w, indicating the better wettability and efficient ion diffusion rooting in the hydrophilic nitrogen-containing groups. The R_{ESR} of NGF-SC is only 2.6 Ω, whereas the R_{ESR} of GF-SC is much larger (11.1 Ω). EIS measurement indicates the better electrochemical resistance behavior of NGF-SC, which is consistent with aforementioned statements.

The total energy stored in supercapacitors is proportional to the square of its operating voltage [48,49]. The application of ionic liquids (IL) as electrolyte is assumed a feasible approach to achieve high operating voltage [6]. So, 1-ethyl-3-methylimidazolium tetrafluoroborate ($EMIMBF_4$) is employed as the electrolyte in our system to increase the potential window up to 0–3.5 V. Nearly symmetrical CV curves with semi-rectangle shape from 10 to 1000 mV s^{-1} reflect excellent capacitive properties of NGF electrodes in IL (Fig. 3e). The GCD curve of NGF electrodes with IL displays semi-straight lines at 1 A g^{-1} (Fig. 3f), resulting C_g of 232 F g^{-1} and C_v of 380 F cm^{-3}. The inset of Fig. 3f shows a red light-emitting diode (LED) powered by one cell composed of symmetric NGF. Benefited from the high potential window, the NGF electrodes perform gravimetric energy density (E_g) of 98 W h kg^{-1} and volumetric energy density (E_v) of 161 W h L^{-1}, with gravimetric power density (P_g) of 875 W kg^{-1} and volumetric power density (P_v) of 1435 W L^{-1}. Compared with other representative supercapacitor electrodes [11,26,50–61], our NGF electrodes with IL show the highest E_v with top-level E_g (Fig. 3g). Even under high power density (8345 W kg^{-1} or 13686 W L^{-1}), the E_g and E_v still retained 61 W h kg^{-1} and 100 W h L^{-1} (Fig. 3h). Therefore, NGF electrodes with IL display outstanding energy storage ability, which is at the highest level compared with carbonaceous electrodes [56,58,61–66]. Notably, the energy density of NGF electrode with H_2SO_4 is also comparable to the top level of carbonaceous electrodes with aqueous electrolytes.

In order to optimize the performance of NGF electrodes, NGF with different hydrothermal time has been studied. The C_g and rate capability of NGF electrodes in Fig. S8 indicate that the best reaction hydrothermal time is 2 h. SEM images indicate the change of the inner structure during the hydrothermal reaction (Fig. S9). The crumpled structure becomes uniformly dispersed in the whole NGF after 1 h reaction, while NGF with 0.5 h reaction has more flat sheets. XPS data shown in Fig. S10 demonstrates that NGF with 2 h reaction has the highest nitrogen content, which is favorable to the electrochemical performance [67].

2.4. Mass loading effects

Given that some essential inactive materials (such as current collectors and separators for the assembly of practical devices) would also contribute certain weight and volume with inactivity, high mass loading of active materials are required to lower the manufacturing cost and guarantee the whole device performance [11,12]. NGFs with different thicknesses ranging from 2 to 70 μm have been fabricated (Fig. 4a, S11). Notably, the NGF displays LOSC structures no matter how thick it is (Fig. 4b, S12). In contrast, high thickness of the GF (such as ~ 20 μm thick in Fig. 4c) may result in serious breakage, due to the huge gas bubbles during reduction. Despite so, the reduced graphene oxide sheets in GF of ~ 20 μm still maintained flat and smooth, due to the serious π-π restacking (Fig. 4d).

The relationship between mass loading and thickness has been ascertained to analyze the effects on NGF density (Fig. 4e). Mass loading is nearly proportional to the thickness, indicating that the density of the NGF stays around 1.64 g cm^{-3} and is hardly affected by thickness. The CV curves in Fig. 4f show a semi-rectangle shape whether under low mass loading (0.32 mg cm^{-2}) or high mass loading (11.2 mg cm^{-2}), indicating good capacitive behavior. Fig. S13 is the GCD curve of $NGF_{11.2}$-SC at 1 A g^{-1} in H_2SO_4, showing low IR drop (~ 0.04 V) and symmetric straight lines which indicates good supercapacitive behavior. The C_gs of the assembled NGF based supercapacitors with different mass loading are shown in Fig. 4g. As the mass loading increases, the C_g almost peeks constant, i.e., 252 F g^{-1} ($NGF_{0.32}$ electrode) to 226 F g^{-1} ($NGF_{11.2}$ electrode). As the thickness increases 35 times from 2 to 70 μm, 90% retention of C_g is achieved. This manifests excellent ion transportation efficiency through the carbon skeleton, underscoring the superiority of the 3H design. Likewise, the areal specific capacitance (C_a) is nearly proportional to the mass loading, and the highest C_a of 2531 mF cm^{-2} was achieved with the mass loading of 11.2 mg cm^{-2} (Fig. 4g). Compared with other highly loaded carbonaceous electrodes, C_a value of 2531 mF cm^{-2} is at the top level [68–71]. Even at high current density of 10 A g^{-1} (Fig. S14), $NGF_{11.2}$ electrode still retains 113 F g^{-1}, demonstrating its high rate capability (50% as the current density increasing 10 times) under high mass loading. This is also due to the good capacitive behavior benefited from the unique LOSC synergetic structures. As a comparison, the density of the GF decreases sharply from 1.47 ± 0.07 to 0.36 ± 0.04 g cm^{-3} when the mass loading increases from 0.3 to 3.7 mg cm^{-2} (Fig. S15), attributed to the big cavities during the hydrothermal reduction (Fig. S16). As a result, the GF-SCs with different mass loading display relatively poor electrochemical performance (191 F g^{-1} for $GF_{0.3}$-SC, 102 F g^{-1} for $GF_{3.7}$-SC) (Fig. S17), indicating that the

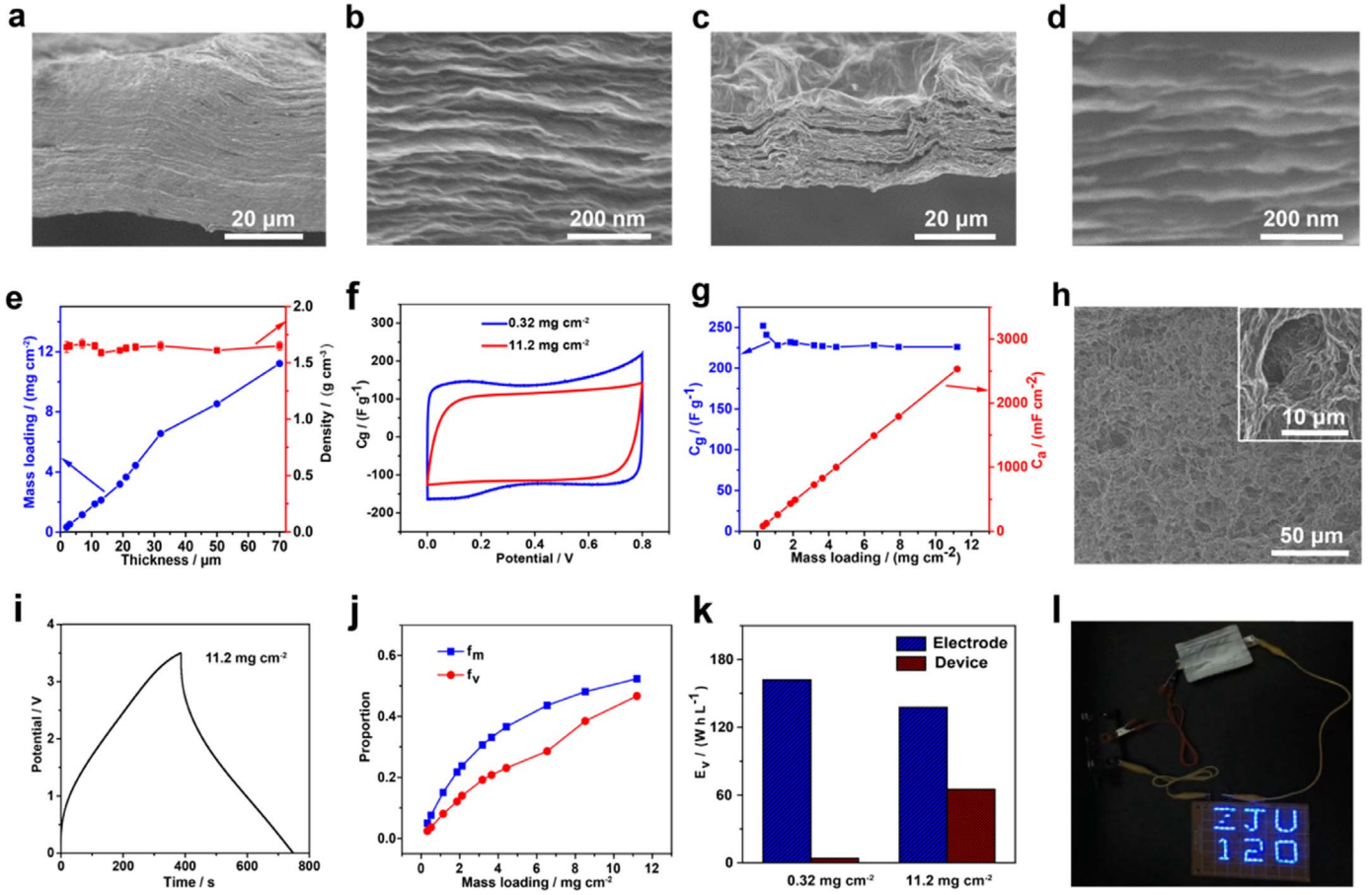

Fig. 4. (a, b) Cross-section SEM images of the NGF with the thickness of ~ 70 μm under different magnifications. (c, d) Cross-section SEM images of the GF with the thickness of ~ 20 μm under different magnifications. (e) Mass loading of the NGF is nearly proportional to the thickness and the densities of NGF are around 1.64 g cm^{-3}. (f) CV curves of $NGF_{0.32}$-SC and $NGF_{11.2}$-SC in 1 M H_2SO_4, the scan rate is 10 mV s^{-1}. (g) Effects of mass loading on C_g and C_a of NGF-SC under the current density of 1 A g^{-1}. (h) Top-view SEM image of the surface of NGF, the inset is the magnified image to show the fissure. (i) The GCD curve of $NGF_{11.2}$-SC with $EMIMBF_4$ at 1 A g^{-1}. (j) Effects of mass loading on f_m and f_v. (k) Effects of mass loading on volumetric performance of electrode and device. (l) 64 blue LEDs powered by one pouch cell assembled from $NGF_{11.2}$ with $EMIMBF_4$.

performance of GF-SCs are largely affected by the thickness. The top-view SEM images shown in Fig. 4h indicate numerous crumples on the surface of the NGF, resulting in channels for ions permeating deeply into the electrodes (the inset in Fig. 4h) [72]. For comparison, GF shows flat and smooth surface (Fig. S18), leading to more difficulty for ions transmission and thus poor electrochemical performance. Overall, the 3H design is an important principle to attain high performance supercapacitors with high mass loading.

We further utilized the $NGF_{11.2}$ to make practical supercapacitors with $EMIMBF_4$, evaluating the gravimetric and volumetric energy density of the whole device ($E_{g\text{-device}}$ and $E_{v\text{-device}}$). According to the CV curve in Fig. S19, the $NGF_{11.2}$-SC still maintains semi-rectangle shape, indicating its good supercapacitive behavior [73]. The $NGF_{11.2}$ electrodes with IL display 215 F g^{-1} and 352 F cm^{-3} at 1 A g^{-1} based on the GCD curve (Fig. 4i), showing E_g of 84 W h kg^{-1} and E_v of 138 W h L^{-1} with the power density of 838 W kg^{-1} and 1374 W L^{-1}, respectively. Even under the high current density of 56 mA cm^{-2}, the $NGF_{11.2}$ electrodes with IL still show 20 W h kg^{-1} or 25 W h L^{-1}. At high mass loading, the mass fraction (f_m) and volume fraction (f_v) of active materials in whole device increase to a high level (Fig. 4j). Compared with $NGF_{0.32}$-SC that f_m and f_v are only 0.05 and 0.024 respectively, $NGF_{11.2}$-SC shows f_m of 0.52 and f_v of 0.47, which means that active materials occupy the main part of the device under high mass loading. The effects of mass loading on the electrode performance and device performance are shown in Fig. 4k and Fig. S20. $NGF_{0.32}$-SC shows high electrode performance (E_g of 98 W h kg^{-1} and E_v of 161 W h L^{-1}) but low device performance ($E_{g\text{-device}}$ of 5 W h kg^{-1} and $E_{v\text{-device}}$ of 4 W h L^{-1}). In comparison, $NGF_{11.2}$-SC both shows high electrode performance (E_g of 84 W h kg^{-1} and E_v of 138 W h L^{-1}) and device performance ($E_{g\text{-device}}$ of 44 W h kg^{-1} and $E_{v\text{-device}}$ of 65 W h L^{-1}), which are much higher than the commercial carbonaceous electrodes based devices (< 10 W h kg^{-1} or 10 W h L^{-1}) shown in Table S4. By utilizing $NGF_{11.2}$ with total mass of ~ 40 mg, one pouch cell lighted up 64 blue light emitting diodes (3–3.4 V of working voltage) for more than 5 min (Fig. 4l), demonstrating the potential practical applications.

2.5. Cycling stability

The cycling stability with high mass loading is another challenge unresolved yet mainly due to the easy fracture of thick electrodes during repeated charging and discharging. Fig. 5a demonstrates that the performance of $NGF_{0.32}$-SC do not decline obviously with nearly 99.6% retention after 100,000 cycling tests in aqueous electrolyte. Similarly, under the high mass loading of 11.2 mg cm^{-2}, the $NGF_{11.2}$-SC still remains 90.1% of its initial capacitance, indicating the high cycling stability with high mass loading. The comparisons of the initial and the 100,000th GCD curves are displayed for both $NGF_{0.32}$-SC and $NGF_{11.2}$-SC in the inset of Fig. 5a respectively. Both of $NGF_{0.32}$-SC and $NGF_{11.2}$-SC did not change much before and after cycling tests, demonstrating the stability of our NGF with different mass loading. Compared with reported supercapacitors of mass loading above 10 mg cm^{-2} [10–15,74,75], our $NGF_{11.2}$-SC shows the longest lifespan (Fig. 5b). In addition, $NGF_{11.2}$-SC with IL has been cycled 50,000 times in potential range of 0–3.5 V (Fig. 5c). 84.8% retention demonstrates the possibility

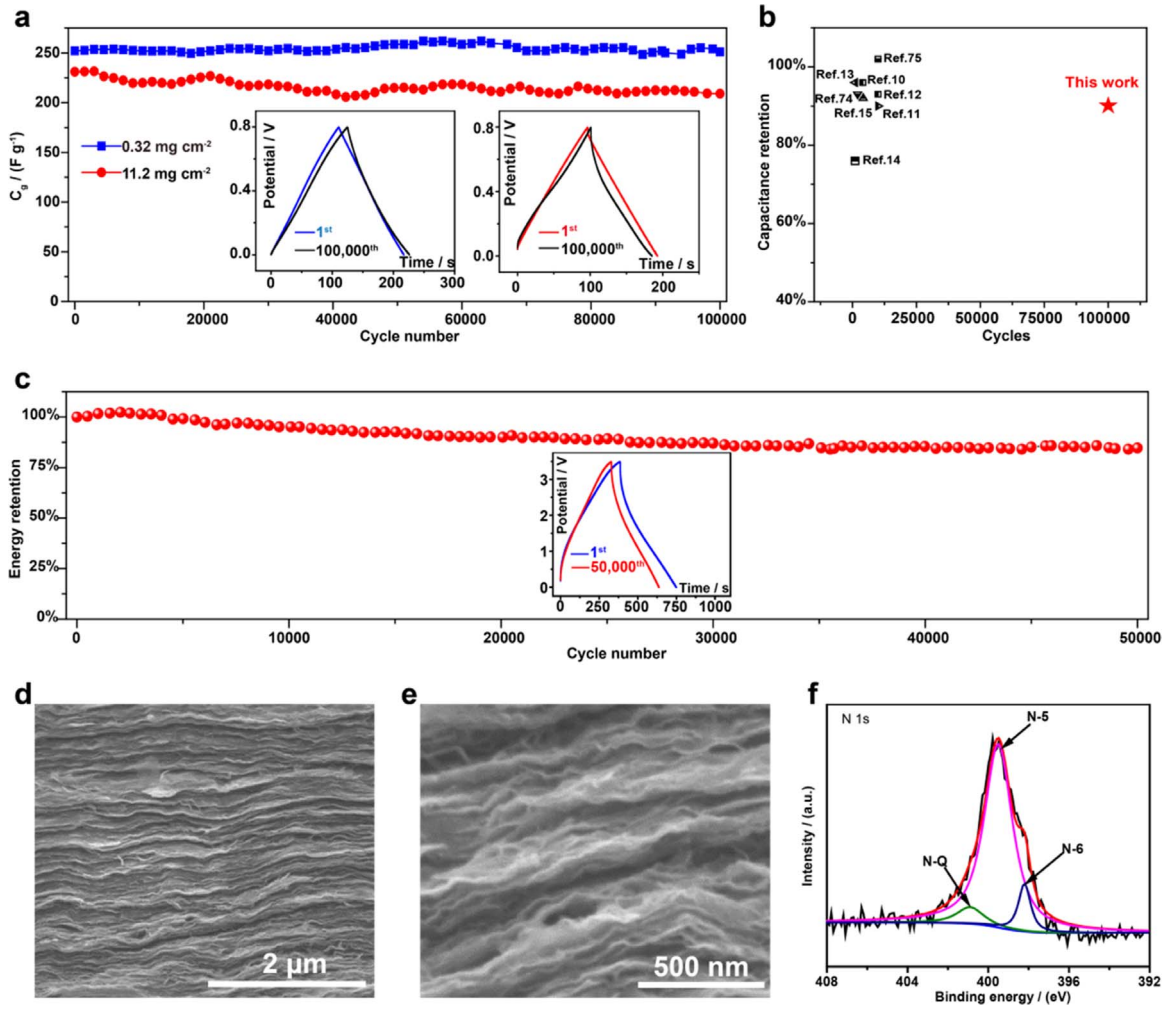

Fig. 5. (a) Cycling stability of $NGF_{0.32}$-SC and $NGF_{11.2}$-SC in aqueous electrolyte, the insets show the 1st and 100,000th GCD curves of $NGF_{0.32}$-SC (left) and $NGF_{11.2}$-SC (right). (b) Comparison of the stability of $NGF_{11.2}$-SC and reported supercapacitor electrodes with mass loading above 10 mg cm^{-2} in 1 M H_2SO_4. (c) Cycling stability of $NGF_{11.2}$-SC in $EMIMBF_4$, the inset shows the 1st and 100,000th GCD curve. (d, e) Cross-section SEM images of the $NGF_{11.2}$ film after 50,000 cycles with $EMIMBF_4$. (f) XPS deconvolutions of the N 1s region of $NGF_{11.2}$ after 50,000 cycles with $EMIMBF_4$.

of the NGF assembled supercapacitors in practical applications. The inset in Fig. 5c indicates the semi-triangle shape is remained after long cycling with few energy lost. The comparisons of electrochemical performances of carbonaceous electrodes with mass loading above 1 mg cm^{-2} are listed in Table S3. Accordingly, $NGF_{11.2}$-SC performs both excellent capacitance and long lifespan under high mass loading compared with these state-of-the-art supercapacitors. After the long cycling tests, the unique LOSC structure still remains well (Fig. 5d, e), without apparent differences compared with the initial structure shown in Fig. 2a, b. The nitrogen content still retained 7.2% after 100,000 cycles, with nearly no obvious changes in N 1 s deconvolutions (Fig. 5f). These cycling tests show the outstanding stability of our NGF-SC, which is essential for practical applications.

3. Conclusions

In summary, a compact yet crumpled nitrogen-doped graphene film is prepared by the guideline of 3H design, which integrates both high density (1.64 ± 0.05 g cm^{-3}) and suitable pore distributions. The NGF exhibits unique LOSC structure, resulting in high electrochemical performance both in aqueous electrolyte and ionic liquid. NGF electrodes performed the highest volumetric energy density (161 W h L^{-1}) in $EMIMBF_4$. Significantly, the performance of NGF electrodes are independent of the electrode thickness, resulting in volumetric energy density 132 W h L^{-1} with mass loading of 11.2 mg cm^{-2}. Such a high mass loading enables the gravimetric and volumetric fraction of active materials in the whole device to reach 0.52 and 0.47 respectively, resulting in 44 W h kg^{-1} and 65 W h L^{-1} of the whole device. The resulting NGF-SCs with high mass loading 11.2 mg cm^{-2} showed 84.8% retention after 50,000 cycles in potential range of 0–3.5 V, and 90.1% retention after 100,000 cycles in aqueous electrolyte. We believe that the 3H design principle can be extended to fabricate other practical supercapacitors with both high energy density and power density.

4. Experimental section

4.1. Materials

All the reagents were of analytical grade and used as received. GO with average lateral size of 2 μm was purchased from www.gaoxitech.com.

4.2. Preparation of NHC-GO

GO aqueous solution (15 mg mL^{-1}) was spun into a coagulation bath (water: ethanol = 3:1, NH_4HCO_3:10 wt%) from a designed flattened nozzle. After 5 min staying, GO was crosslinked and became hydrogel film named NHC-GO, which was collected by the winders.

4.3. Preparation of NGF

NHC-GO hydrogel film was transferred into a closed Teflon-lined autoclave full-filled with aqueous bath (NH_4HCO_3, 10 wt%) and heated at 180 °C for a suitable time (2 h if no specific statement). The obtained black NGF was washed with water and stayed under the pressure of 10 MPa for one night air-drying.

By utilizing different hydrothermal time (0.5, 1, 2, 3, 5, 8 and 18 h), NGF was fabricated with different reduction degree and nitrogen doping degree.

By utilizing nozzles with different sizes, NGF was fabricated with different thickness and thus different mass loading. For example, with the nozzle of thickness of 50 μm, NGF was fabricated with the mass loading of 0.32 mg cm^{-2}, and it was named $NGF_{0.32}$.

4.4. Preparation of GF

NHC-GO hydrogel film was heated at 80 °C in pure water for 12 h to decompose NH_4HCO_3. Then, the film was transferred into the deionized water contained autoclaves and heated at 180 °C for 2 h. The obtained black GF was washed with water and stayed air-drying under the pressure of 10 MPa for one night air-drying.

By utilizing nozzles with different sizes, GF was fabricated with different thickness and thus different mass loading. For example, with the nozzle of thickness of 50 μm, GF was fabricated with the mass loading of 0.3 mg cm^{-2}, and it was named $GF_{0.3}$.

4.5. Characterization

SEM tests were measured by Hitachi S-4800. XRD was conducted on Rigaku D/max-2500, using graphite monochromatized CuK α radiation. XPS measurements were acquired by a PHI 5000 C ESCA system (Physical Electronics) operated at 14.0 kV. Mechanical property tests were carried on a HS-3002C at a loading rate of 10% per minute. Electrochemical measurements were performed in cells with two symmetrical electrodes, using a MPF30AC membrane (thickness of 100 μm, areal density of 3 mg cm^{-2}) from Nippon Kodoshi Corporation as separator. A commercial graphite film (thickness of 30 μm, areal density of 6 mg cm^{-2}) is used as the current collector. 1 M H_2SO_4 was used as the aqueous electrolyte to achieve working voltage window of 0–0.8 V, and $EMIMBF_4$ was used as the organic electrolyte to achieve working potential window of 0–3.5 V. CV and GCD tests were carried out using an electrochemical workstation (CHI660e, CH Instruments, Inc.). EIS tests were measured on Multi Autolab M204 (Metrohm).

4.6. Calculation

(1) The gravimetric specific capacitance calculated by CV:

$$C_g = \frac{\oint IdU}{m \times u \times (U2 - U1)}$$

where C_g (F g^{-1}), m (g), u (V s^{-1}), U_2 and U_1 (V), and I (A) are the gravimetric specific capacitance, the weight of single electrode, scan rate, high and low potential limit of CV tests, and the instant current of CV curves, respectively.

(2) The gravimetric specific capacitance calculated by GCD:

$$C_g = \frac{2 \times I \times t}{m \times \Delta U}$$

where C_g (F g^{-1}), I (A), t (s), ΔU (V), and m (g) are the gravimetric specific capacitance, the discharge current, the discharge time, the potential window and the weight of single electrode, respectively.

(3) The volumetric specific capacitance is calculated as followed:

$$C_v = C_g \times \rho$$

where C_v (F cm^{-3}) and ρ (g cm^{-3}) are volumetric specific capacitance of one electrode and the density of one electrode, respectively.

The areal specific capacitance is calculated as followed:

$$C_a = C_g \times m_l$$

where C_a (mF cm^{-2}) and m_l (mg cm^{-2}) are areal specific capacitance of one electrode and the mass loading of one electrode, respectively.

(4) The gravimetric energy density and power density are calculated as followed:

$$Eg = \frac{1}{3.6 \times 8} C_g U^2$$

$$Pg = \frac{Eg}{t}$$

where E_g (W h kg^{-1}), C_g (F g^{-1}), U (V), P_g (W kg^{-1}), t (h) are the gravimetric energy density, the gravimetric specific capacitance, the potential window, the gravimetric power density and the discharge time, respectively.

(5) The volumetric energy density and power density are calculated as followed:

$$Ev = Eg \times \rho$$

$$Pv = Pg \times \rho$$

where E_v (W h L^{-1}) and P_v (W L^{-1}) are the volumetric energy density and the volumetric power density, respectively.

(6) The gravimetric and volumetric energy density of the whole device are calculated as followed:

$$E_{g-device} = E_g \times f_m$$

$$E_{v-device} = E_v \times f_v$$

where $E_{g\text{-device}}$ (W h kg^{-1}) and $E_{v\text{-device}}$ (W h L^{-1}) are the gravimetric energy density and volumetric energy density of the whole device including current collector, electrolyte, separator and active materials, respectively. f_m and f_v are the mass and volume fraction of the two electrodes in the cell, respectively.

Acknowledgments

This work is supported by the National Natural Science Foundation of China (Nos. 51533008, 21325417 and 51703194), National Key R & D Program of China (No. 2016YFA0200200), Fundamental Research Funds for the Central Universities (Nos. 2017QNA4036 and 2017XZZX008-06), and Hundred Talents Program of Zhejiang University (188020*194231701/113).

Appendix B. Supporting information

Supplementary data associated with this article can be found in the online version at doi:10.1016/j.ensm.2018.07.001.

References

[1] C. Liu, F. Li, L.-P. Ma, H.-M. Cheng, Advanced materials for energy storage, Adv. Mater. 22 (8) (2010) E28–E62.
[2] A.S. Aricò, P. Bruce, B. Scrosati, J.-M. Tarascon, W. van Schalkwijk, Nanostructured materials for advanced energy conversion and storage devices, Nat. Mater. 4 (2005) 366.
[3] R. Kötz, M. Carlen, Principles and applications of electrochemical capacitors, Electrochim. Acta 45 (15–16) (2000) 2483–2498.
[4] A. Burke, Ultracapacitors: why, how, and where is the technology, J. Power Sources 91 (1) (2000) 37–50.

[5] M. Winter, R.J. Brodd, What are batteries, fuel cells, and supercapacitors?, Chem. Rev. 104 (10) (2004) 4245–4270.
[6] C. Li, X. Zhang, K. Wang, X. Sun, G. Liu, J. Li, H. Tian, J. Li, Y. Ma, Scalable self-propagating high-temperature synthesis of graphene for supercapacitors with superior power density and cyclic stability, Adv. Mater. 29 (2017) 1604690.
[7] J. Zhao, Y. Jiang, H. Fan, M. Liu, O. Zhuo, X. Wang, Q. Wu, L. Yang, Y. Ma, Z. Hu, Porous 3D few-layer graphene-like carbon for ultrahigh-power supercapacitors with well-defined structure–performance relationship, Adv. Mater. 29 (2017) 1604569.
[8] Z. Li, Z. Xu, H. Wang, J. Ding, B. Zahiri, C.M.B. Holt, X. Tan, D. Mitlin, Colossal pseudocapacitance in a high functionality-high surface area carbon anode doubles the energy of an asymmetric supercapacitor, Energy Environ. Sci. 7 (5) (2014) 1708–1718.
[9] L. Hao, B. Luo, X. Li, M. Jin, Y. Fang, Z. Tang, Y. Jia, M. Liang, A. Thomas, J. Yang, L. Zhi, Terephthalonitrile-derived nitrogen-rich networks for high performance supercapacitors, Energy Environ. Sci. 5 (12) (2012) 9747–9751.
[10] Y. Tao, X. Xie, W. Lv, D.-M. Tang, D. Kong, Z. Huang, H. Nishihara, T. Ishii, B. Li, D. Golberg, F. Kang, T. Kyotani, Q.-H. Yang, Towards ultrahigh volumetric capacitance: graphene derived highly dense but porous carbons for supercapacitors, Sci. Rep. 3 (2013) 2975.
[11] H. Li, Y. Tao, X. Zheng, J. Luo, F. Kang, H.-M. Cheng, Q.-H. Yang, Ultra-thick graphene bulk supercapacitor electrodes for compact energy storage, Energy Environ. Sci. 9 (10) (2016) 3135–3142.
[12] C. Chen, Y. Zhang, Y. Li, J. Dai, J. Song, Y. Yao, Y. Gong, I. Kierzewski, J. Xie, L. Hu, All-wood, low tortuosity, aqueous, biodegradable supercapacitors with ultrahigh capacitance, Energy Environ. Sci. 10 (2) (2017) 538–545.
[13] Z.Y. Lu, Q. Yang, W. Zhu, Z. Chang, J.F. Liu, X.M. Sun, D.G. Evans, X. Duan, Hierarchical Co3O4@Ni-Co-O supercapacitor electrodes with ultrahigh specific capacitance per area, Nano Res. 5 (5) (2012) 369–378.
[14] C.H. Tang, X.S. Yin, H. Gong, Superior performance asymmetric supercapacitors based on a directly grown commercial mass 3D Co3O4@Ni(OH)(2) core-shell electrode, ACS Appl. Mater. Interfaces 5 (21) (2013) 10574–10582.
[15] X. Zhang, J.S. Luo, P.Y. Tang, X.L. Ye, X.X. Peng, H.L. Tang, S.G. Sun, J. Fransaer, A universal strategy for metal oxide anchored and binder-free carbon matrix electrode: a supercapacitor case with superior rate performance and high mass loading, Nano Energy 31 (2017) 311–321.
[16] Y. Xia, T.S. Mathis, M.-Q. Zhao, B. Anasori, A. Dang, Z. Zhou, H. Cho, Y. Gogotsi, S. Yang, Thickness-independent capacitance of vertically aligned liquid-crystalline MXenes, Nature 557 (7705) (2018) 409–412.
[17] B. Yongfeng, S. Tao, C. Yuejin, D. Lingyu, Z. Ou, Y. Lijun, W. Qiang, W. Xizhang, H. Zheng, Compressing carbon nanocages by capillarity for optimizing porous structures toward ultrahigh-volumetric-performance supercapacitors, Adv. Mater. 29 (24) (2017) 1700470.
[18] D. Feng, T. Lei, M.R. Lukatskaya, J. Park, Z. Huang, M. Lee, L. Shaw, S. Chen, A.A. Yakovenko, A. Kulkarni, J. Xiao, K. Fredrickson, J.B. Tok, X. Zou, Y. Cui, Z. Bao, Robust and conductive two-dimensional metal–organic frameworks with exceptionally high volumetric and areal capacitance, Nat. Energy 3 (1) (2018) 30–36.
[19] L. Hu, W. Chen, X. Xie, N. Liu, Y. Yang, H. Wu, Y. Yao, M. Pasta, H.N. Alshareef, Y. Cui, Symmetrical MnO2–carbon nanotube–textile nanostructures for wearable pseudocapacitors with high mass loading, ACS Nano 5 (11) (2011) 8904–8913.
[20] Y.M. He, W.J. Chen, X.D. Li, Z.X. Zhang, J.C. Fu, C.H. Zhao, E.Q. Xie, Freestanding three-dimensional graphene/MnO2 composite networks as ultra light and flexible supercapacitor electrodes, ACS Nano 7 (1) (2013) 174–182.
[21] K.A. Owusu, L.B. Qu, J.T. Li, Z.Y. Wang, K.N. Zhao, C. Yang, K.M. Hercule, C. Lin, C.W. Shi, Q.L. Wei, L. Zhou, L.Q. Mai, Low-crystalline iron oxide hydroxide nanoparticle anode for high-performance supercapacitors, Nat. Commun. 8 (2017).
[22] Z. Lei, J. Zhang, L.L. Zhang, N.A. Kumar, X.S. Zhao, Functionalization of chemically derived graphene for improving its electrocapacitive energy storage properties, Energy Environ. Sci. 9 (6) (2016) 1891–1930.
[23] J.Y. Luo, H.D. Jang, J.X. Huang, Effect of sheet morphology on the scalability of graphene-based ultracapacitors, ACS Nano 7 (2) (2013) 1464–1471.
[24] T. Lin, I.-W. Chen, F. Liu, C. Yang, H. Bi, F. Xu, F. Huang, Nitrogen-doped mesoporous carbon of extraordinary capacitance for electrochemical energy storage, Science 350 (6267) (2015) 1508–1513.
[25] C. Zhang, W. Lv, Y. Tao, Q.-H. Yang, Towards superior volumetric performance: design and preparation of novel carbon materials for energy storage, Energy Environ. Sci. 8 (5) (2015) 1390–1403.
[26] X. Yang, C. Cheng, Y. Wang, L. Qiu, D. Li, Liquid-mediated dense integration of graphene materials for compact capacitive energy storage, Science 341 (6145) (2013) 534–537.
[27] Z. Xu, C. Gao, Aqueous liquid crystals of graphene oxide, ACS Nano 5 (4) (2011) 2908–2915.
[28] Z. Xu, C. Gao, Graphene chiral liquid crystals and macroscopic assembled fibres, Nat. Commun. 2 (2011) 571.
[29] Z. Liu, Z. Li, Z. Xu, Z. Xia, X. Hu, L. Kou, L. Peng, Y. Wei, C. Gao, Wet-spun continuous graphene films, Chem. Mater. 26 (23) (2014) 6786–6795.
[30] M.D. Stoller, S. Park, Y. Zhu, J. An, R.S. Ruoff, Graphene-based ultracapacitors, Nano Lett. 8 (10) (2008) 3498–3502.
[31] X. Zhang, Z. Sui, B. Xu, S. Yue, Y. Luo, W. Zhan, B. Liu, Mechanically strong and highly conductive graphene aerogel and its use as electrodes for electrochemical power sources, J. Mater. Chem. 21 (18) (2011) 6494–6497.
[32] J.-S. Lee, S.-I. Kim, J.-C. Yoon, J.-H. Jang, Chemical vapor deposition of mesoporous graphene nanoballs for supercapacitor, ACS Nano 7 (7) (2013) 6047–6055.
[33] X. Yang, J. Zhu, L. Qiu, D. Li, Bioinspired effective prevention of restacking in multilayered graphene films: towards the next generation of high-performance supercapacitors, Adv. Mater. 23 (25) (2011) 2833–2838.
[34] D.A. Dikin, S. Stankovich, E.J. Zimney, R.D. Piner, G.H.B. Dommett, G. Evmenenko, S.T. Nguyen, R.S. Ruoff, Preparation and characterization of graphene oxide paper, Nature 448 (7152) (2007) 457–460.
[35] H. Chen, M.B. Müller, K.J. Gilmore, G.G. Wallace, D. Li, Mechanically strong, electrically conductive, and biocompatible graphene paper, Adv. Mater. 20 (18) (2008) 3557–3561.
[36] Y. Xu, H. Bai, G. Lu, C. Li, G. Shi, Flexible graphene films via the filtration of water-soluble noncovalent functionalized graphene sheets, J. Am. Chem. Soc. 130 (18) (2008) 5856–5857.
[37] T. Huang, B. Zheng, Z. Liu, L. Kou, C. Gao, High rate capability supercapacitors assembled from wet-spun graphene films with a CaCO3 template, J. Mater. Chem. A 3 (5) (2015) 1890–1895.
[38] C. Bommier, T.W. Surta, M. Dolgos, X. Ji, New mechanistic insights on Na-Ion storage in nongraphitizable carbon, Nano Lett. 15 (9) (2015) 5888–5892.
[39] Y. Xu, Y. Tao, X. Zheng, H. Ma, J. Luo, F. Kang, Q.-H. Yang, A. Metal-Free Supercapacitor, Electrode material with a record high volumetric capacitance over 800 F cm−3, Adv. Mater. 27 (48) (2015) 8082–8087.
[40] L. Peng, Z. Xu, Z. Liu, Y. Guo, P. Li, C. Gao, Ultrahigh thermal conductive yet superflexible graphene films, Adv. Mater. 29 (27) (2017) (1700589-n/a).
[41] D. Hulicova-Jurcakova, M. Seredych, G.Q. Lu, T.J. Bandosz, Combined effect of nitrogen- and oxygen-containing functional groups of microporous activated carbon on its electrochemical performance in supercapacitors, Adv. Funct. Mater. 19 (3) (2009) 438–447.
[42] L. Qie, W. Chen, H. Xu, X. Xiong, Y. Jiang, F. Zou, X. Hu, Y. Xin, Z. Zhang, Y. Huang, Synthesis of functionalized 3D hierarchical porous carbon for high-performance supercapacitors, Energy Environ. Sci. 6 (8) (2013) 2497–2504.
[43] C. Petit, M. Seredych, T.J. Bandosz, Revisiting the chemistry of graphite oxides and its effect on ammonia adsorption, J. Mater. Chem. 19 (48) (2009) 9176–9185.
[44] W. He, L. Lu, Revisiting the structure of graphene oxide for preparing new-style graphene-based ultraviolet absorbers, Adv. Funct. Mater. 22 (12) (2012) 2542–2549.
[45] D.-W. Wang, F. Li, L.-C. Yin, X. Lu, Z.-G. Chen, I.R. Gentle, G.Q. Lu, H.-M. Cheng, Nitrogen-doped carbon monolith for alkaline supercapacitors and understanding nitrogen-induced redox transitions, Chem. – A Eur. J. 18 (17) (2012) 5345–5351.
[46] V. Khomenko, E. Frackowiak, F. Béguin, Determination of the specific capacitance of conducting polymer/nanotubes composite electrodes using different cell configurations, Electrochim. Acta 50 (12) (2005) 2499–2506.
[47] B. Hsia, J. Marschewski, S. Wang, J.B. In, C. Carraro, D. Poulikakos, C.P. Grigoropoulos, R. Maboudian, Highly flexible, all solid-state micro-supercapacitors from vertically aligned carbon nanotubes, Nanotechnology 25 (5) (2014).
[48] Z. Fan, J. Yan, T. Wei, L. Zhi, G. Ning, T. Li, F. Wei, Asymmetric supercapacitors based on graphene/MnO2 and activated carbon nanofiber electrodes with high power and energy density, Adv. Funct. Mater. 21 (12) (2011) 2366–2375.
[49] J. Yan, Z. Fan, W. Sun, G. Ning, T. Wei, Q. Zhang, R. Zhang, L. Zhi, F. Wei, Advanced asymmetric supercapacitors based on Ni(OH)2/graphene and porous graphene electrodes with high energy density, Adv. Funct. Mater. 22 (12) (2012) 2632–2641.
[50] J. Yan, Q. Wang, C. Lin, T. Wei, Z. Fan, Interconnected frameworks with a sandwiched porous carbon layer/graphene hybrids for supercapacitors with high gravimetric and volumetric performances, Adv. Energy Mater. 4 (13) (2014) (1400500-n/a).
[51] J. Hu, H. Wang, Q. Gao, H. Guo, Porous carbons prepared by using metal–organic framework as the precursor for supercapacitors, Carbon 48 (12) (2010) 3599–3606.
[52] L. Zhang, F. Zhang, X. Yang, K. Leng, Y. Huang, Y. Chen, High-performance supercapacitor electrode materials prepared from various pollens, Small 9 (8) (2013) 1342–1347.
[53] S. Murali, N. Quarles, L.L. Zhang, J.R. Potts, Z. Tan, Y. Lu, Y. Zhu, R.S. Ruoff, Volumetric capacitance of compressed activated microwave-expanded graphite oxide (a-MEGO) electrodes, Nano Energy 2 (5) (2013) 764–768.
[54] Y. Li, Z. Li, P.K. Shen, Simultaneous formation of ultrahigh surface area and three-dimensional hierarchical porous graphene-like networks for fast and highly stable supercapacitors, Adv. Mater. 25 (17) (2013) 2474–2480.
[55] J. Hu, Z. Kang, F. Li, X. Huang, Graphene with three-dimensional architecture for high performance supercapacitor, Carbon 67 (Suppl. C) (2014) S221–S229.
[56] J. Yan, Q. Wang, T. Wei, L. Jiang, M. Zhang, X. Jing, Z. Fan, Template-assisted low temperature synthesis of functionalized graphene for ultrahigh volumetric performance supercapacitors, ACS Nano 8 (5) (2014) 4720–4729.
[57] Y. Xu, Z. Lin, X. Zhong, X. Huang, N.O. Weiss, Y. Huang, X. Duan, Holey graphene frameworks for highly efficient capacitive energy storage, Nat. Commun. 5 (2014) 4554.
[58] D.T. Pham, T.H. Lee, D.H. Luong, F. Yao, A. Ghosh, V.T. Le, T.H. Kim, B. Li, J. Chang, Y.H. Lee, Carbon nanotube-bridged graphene 3D building blocks for ultrafast compact supercapacitors, ACS Nano 9 (2) (2015) 2018–2027.
[59] M. Acerce, D. Voiry, M. Chhowalla, Metallic 1T phase MoS2 nanosheets as supercapacitor electrode materials, Nat. Nano 10 (4) (2015) 313–318.
[60] M. Ghidiu, M.R. Lukatskaya, M.-Q. Zhao, Y. Gogotsi, M.W. Barsoum, Conductive two-dimensional titanium carbide /`clay/' with high volumetric capacitance, Nature 516 (7529) (2014) 78–81.
[61] Y. Zhu, S. Murali, M.D. Stoller, K.J. Ganesh, W. Cai, P.J. Ferreira, A. Pirkle, R.M. Wallace, K.A. Cychosz, M. Thommes, D. Su, E.A. Stach, R.S. Ruoff, Carbon-based supercapacitors produced by activation of graphene, Science 332 (6037) (2011) 1537–1541.

[62] X. Yan, Y. Yu, S.-K. Ryu, J. Lan, X. Jia, X. Yang, Simple and scalable synthesis of phosphorus and nitrogen enriched porous carbons with high volumetric capacitance, Electrochim. Acta 136 (2014) 466–472.
[63] J. Wang, M. Chen, C. Wang, J. Wang, J. Zheng, Preparation of mesoporous carbons from amphiphilic carbonaceous material for high-performance electric double-layer capacitors, J. Power Sources 196 (1) (2011) 550–558.
[64] Z. Lei, L. Lu, X.S. Zhao, The electrocapacitive properties of graphene oxide reduced by urea, Energy Environ. Sci. 5 (4) (2012) 6391–6399.
[65] Y. Yoon, K. Lee, S. Kwon, S. Seo, H. Yoo, S. Kim, Y. Shin, Y. Park, D. Kim, J.-Y. Choi, H. Lee, Vertical alignments of graphene sheets spatially and densely piled for fast ion diffusion in compact supercapacitors, ACS Nano 8 (5) (2014) 4580–4590.
[66] L. Zhang, F. Zhang, X. Yang, G. Long, Y. Wu, T. Zhang, K. Leng, Y. Huang, Y. Ma, A. Yu, Y. Chen, Porous 3D graphene-based bulk materials with exceptional high surface area and excellent conductivity for supercapacitors, Sci. Rep. 3 (2013) 1408.
[67] M. Yang, Z. Zhou, Recent breakthroughs in supercapacitors boosted by nitrogen-rich porous carbon materials, Adv. Sci. (2017) (n/a-n/a).
[68] L.-F. Chen, Z.-H. Huang, H.-W. Liang, W.-T. Yao, Z.-Y. Yu, S.-H. Yu, Flexible all-solid-state high-power supercapacitor fabricated with nitrogen-doped carbon nanofiber electrode material derived from bacterial cellulose, Energy Environ. Sci. 6 (11) (2013) 3331–3338.
[69] Z.-S. Wu, S. Yang, L. Zhang, J.B. Wagner, X. Feng, K. Müllen, Binder-free activated graphene compact films for all-solid-state micro-supercapacitors with high areal and volumetric capacitances, Energy Storage Mater. 1 (2015) 119–126.
[70] M.F. El-Kady, V. Strong, S. Dubin, R.B. Kaner, Laser scribing of high-performance and flexible graphene-based electrochemical capacitors, Science 335 (6074) (2012) 1326–1330.
[71] P. Huang, C. Lethien, S. Pinaud, K. Brousse, R. Laloo, V. Turq, M. Respaud, A. Demortière, B. Daffos, P.L. Taberna, B. Chaudret, Y. Gogotsi, P. Simon, On-chip and freestanding elastic carbon films for micro-supercapacitors, Science 351 (6274) (2016) 691–695.
[72] H. Chen, H. Xu, S. Wang, T. Huang, J. Xi, S. Cai, F. Guo, Z. Xu, W. Gao, C. Gao, Ultrafast all-climate aluminum-graphene battery with quarter-million cycle life, Sci. Adv. 3 (12) (2017).
[73] Z. Bo, W. Zhu, W. Ma, Z. Wen, X. Shuai, J. Chen, J. Yan, Z. Wang, K. Cen, X. Feng, Vertically oriented graphene bridging active-layer/current-collector interface for ultrahigh rate supercapacitors, Adv. Mater. 25 (40) (2013) 5799–5806.
[74] Y. Shi, L.J. Pan, B.R. Liu, Y.Q. Wang, Y. Cui, Z.A. Bao, G.H. Yu, Nanostructured conductive polypyrrole hydrogels as high-performance, flexible supercapacitor electrodes, J. Mater. Chem. A 2 (17) (2014) 6086–6091.
[75] H.L. Wang, C.M.B. Holt, Z. Li, X.H. Tan, B.S. Amirkhiz, Z.W. Xu, B.C. Olsen, T. Stephenson, D. Mitlin, Graphene-nickel cobaltite nanocomposite asymmetrical supercapacitor with commercial level mass loading, Nano Res. 5 (9) (2012) 605–617.